nature communications

Article

https://doi.org/10.1038/s41467-025-57140-x

Visible-light-driven CO_2 photoreduction over atomically strained indium sites in ambient air

Received: 21 July 2024

Accepted: 8 February 2025

Published online: 01 March 2025

Check for updates

Kai Wang[1] ✉, Yanjun Hu[1], Xiufan Liu[1], Jun Li[2] ✉ & Bin Liu[3,4] ✉

Strain engineering offers an attractive strategy for improving intrinsic catalytic performance of a heterogeneous catalyst. Herein, we successfully create strain into layered indium sulfide (In_2S_3) at atomic scale via introducing oxygen coordination and sulfur vacancy using a wet-chemistry method. The atomically strained In_2S_3 exhibits greatly enhanced CO_2 photoreduction performance, achieving a CO_2 to CO conversion rate of 5.16 μmol $g_{catalyst}^{-1}$ h^{-1} under visible light illumination in ambient air. In-situ spectroscopic measurements together with theoretical calculations indicate that the atomically strained In_2S_3 features lattice disordered defects on surface, which provides rich uncoordinated catalytic sites and induces structural distortion, resulting in modified band structure that promotes CO_2 adsorption/activation and boosts photogenerated charge carriers' separation during CO_2 photoreduction. This work provides a new approach for the rational design of atomically strained photocatalysts for CO_2 reduction in ambient air.

Solar-driven CO_2 reduction to yield high value-added fuels or chemicals is considered as a highly attractive and promising approach to ameliorate global warming issues associated with enduring CO_2 emissions[1–5]. However, efficient CO_2 photoreduction with high selectivity and stability remains a critical issue because of the high dissociation energy of the C=O bond (ca. 750 kJ mol^{-1}) and the kinetically sluggish multiple-electron-transfer reaction process[6–8]. The CO_2 concentration in the exhaust gases discharged from industries, such as coal-fired power stations is relatively low, restricting practical implementation of CO_2 photoreduction[9–11]. Designing an effective strategy to boost the low-concentration CO_2 molecular activation and improve the CO_2 conversion efficiency has become the key challenges in CO_2 photoreduction.

Metal sulfides have tunable surficial electronic structures owing to their adjustable metal valence states, which have been extensively applied in photocatalytic CO_2 reduction reaction[12–19]. Two-dimensional (2D) metal sulfides exhibit high specific surface areas, which shall benefit photocatalytic reactions by offering a large number of catalytically active sites. Moreover, the ultrathin architecture of these 2D materials can also significantly shorten the migration pathways of photogenerated charge carriers, thereby substantially reducing electron-hole recombination and improving efficiency of charge carrier separation. To further improve the performance of metal sulfide photocatalysts in photocatalysis, tuning electronic structure of metal sites by strain engineering provides an effective strategy[20–31]. Strain engineering of nanomaterials can be mainly achieved by engendering interfacial mismatch or deformation. These methods can induce long-range lattice strain but are not applicable for manipulating the strain environment around specific atomic sites in a short range[32–47]. On the other hand, modulating chemical environment around metal cations may provide an innovative strategy to adjust strain on the atomic scale (Fig. 1a).

In this work, we developed a wet-chemistry method to introduce oxygen coordination and sulfur vacancy into In_2S_3, which induced a

[1]College of Urban and Environmental Sciences, Hubei Key Laboratory of Pollutant Analysis and Reuse Technology, Hubei Normal University, Huangshi, PR China. [2]Henan Institute of Advanced Technology, Zhengzhou University, Zhengzhou, PR China. [3]Department of Materials Science and Engineering, City University of Hong Kong, Hong Kong SAR, PR China. [4]Department of Chemistry, Hong Kong Institute of Clean Energy (HKICE) & Center of Super-Diamond and Advanced Films (COSDAF), City University of Hong Kong, Hong Kong SAR, PR China. ✉e-mail: wangkai@hbnu.edu.cn; junli2019@zzu.edu.cn; bliu48@cityu.edu.hk

https://doi.org/10.1038/s41467-025-57140-x

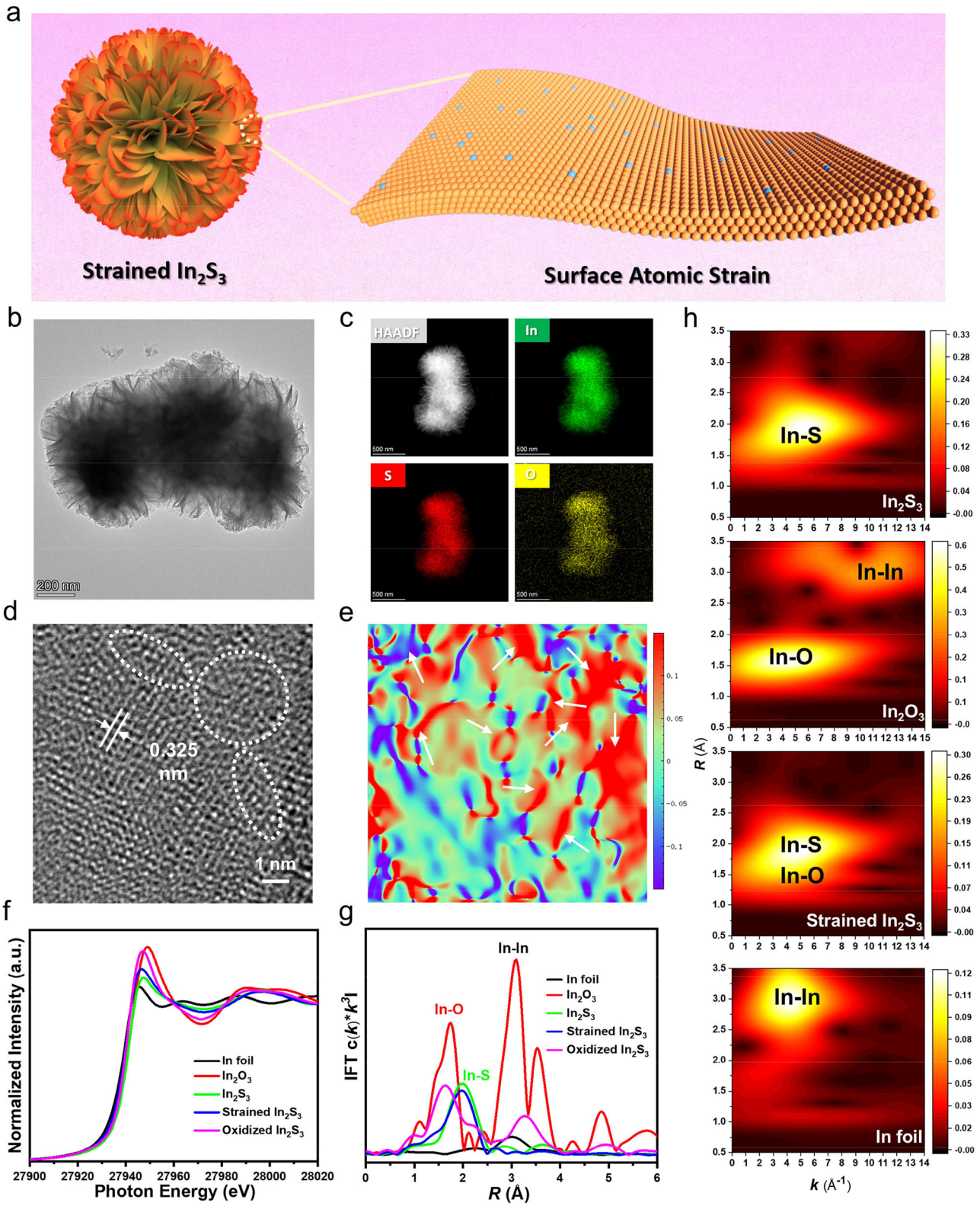

Fig. 1 | Structural characterizations. a Schematic illustration of atomically strained metal-site catalyst. **b** TEM image. **c** HAADF-STEM image and the corresponding elemental mapping images. **d** HRTEM image and **e** the corresponding strain mapping image along the ε_{xx} direction by GPA. **f** XANES and **g** FT-EXAFS spectra recorded in the In *K*-edge. **h** WT-EXAFS plots of In_2S_3, In_2O_3, strained In_2S_3 and oxidized In_2S_3. Source data for Fig. 1f,g are provided as a Source Data file.

small-domain strain at the atomic scale (strained In_2S_3, Fig. 1a). The as-prepared atomically strained In_2S_3 exhibited approximately 9 times higher photocatalytic activity than pristine In_2S_3, towards converting CO_2 to CO in ambient air under visible light irradiation. Based on a collection of in-situ spectroscopic measurements and density functional theory (DFT) calculations, the atomically strained In_2S_3 was found capable to promote CO_2 adsorption/activation and at the same time boost photogenerated charge carrier separation, as a result,

greatly enhancing CO_2 photoreduction performance under full spectrum/visible light illumination in both pure CO_2 and ambient air environment.

Results and discussion

Structural characterizations of layered In_2S_3 with atomically strained Indium sites

Oxygen coordination and sulfur vacancy were introduced into In_2S_3 via a facile one-step solvothermal reaction, in which the induced strain degree in In_2S_3 could be well controlled by the volumetric ratio of water and ethylene glycol used in the solvothermal reaction (Supplementary Fig. 1). X-ray diffraction (XRD) patterns (Supplementary Fig. 2) of the as-prepared pristine In_2S_3 and strained In_2S_3 belong to cubic-phase In_2S_3 (PDF #65-0459)[46]. The (311) diffraction peak of strained In_2S_3 displayed a shift to lower 2θ angles as compared to pristine In_2S_3, indicating possible presence of local structural disorder and strain in the strained In_2S_3. Scanning electron microscopy (SEM) and transmission electron microscopy (TEM) images as displayed in Supplementary Fig. 3, Fig. 1b and Supplementary Fig. 4 showed that both of the pristine In_2S_3 and strained In_2S_3 exhibited flower-like morphology assembled from thin nanosheets. Elemental mapping images indicated homogeneous distribution of In, S and O elements (Fig. 1c) in strained In_2S_3. As illustrated in high-resolution TEM (HR-TEM) image (Fig. 1d and Supplementary Fig. 5), the strained In_2S_3 possessed moderate crystallinity with a fine lattice spacing of 0.325 nm, assignable to the (311) plane of cubic In_2S_3. Figure 1e and Supplementary Fig. 6 showed the strain maps obtained by geometric phase analysis (GPA). Figure 1e displayed the strain distribution around the lattice disorder defects (white circles in Fig. 1d), which showed widespread compression strain around 7%, with some regions reaching 10%. The marked arrows indicated the atomic-level distortion at the lattice, confirming the atomically strained surficial In sites[33]. Supplementary Fig. 7 showed the strain distribution around the lattice disorder areas of oxidized In_2S_3. The oxygen atoms partially replaced the In-S bonds in layered In_2S_3, which in turn creates significant tensile stress. For comparison, pristine In_2S_3 and In_2O_3 were also analyzed by GPA, and both of pristine In_2S_3 and In_2O_3 displayed good crystallinity with ultrathin sheet-like morphologies as presented in Supplementary Fig. 8-9. X-ray photoelectron spectroscopy (XPS) spectra (Supplementary Fig. 10) indicated decreased S 2*p* XPS peak and enhanced O 1*s* XPS peak in strained In_2S_3 as compared to pristine In_2S_3, suggesting that strain creation was associated with In-O bond formation. The same conclusion can be drawn from the observed shift of S 2*p* and In 3*d* XPS peaks to higher binding energies in strained In_2S_3[12]. It is observed that the intensity of O 1*s* XPS peak gradually reduced with increasing Ar^+ sputtering time (Supplementary Fig. 11), corroborating that the O^{2-} ions were introduced into the surface of strained In_2S_3 by replacing S^{2-} ions in In-S bonds[48,49].

The atomic and electronic structures of different In_2S_3 samples were further examined by X-ray absorption spectroscopy (XAS). All samples showed similar pre-edge peaks at about 27935 eV in the In *K*-edge X-ray absorption near-edge structure (XANEs) spectra, suggesting similar In atomic arrangements (Fig. 1f). As displayed in the Fourier-transformed (FT) In *K*-edge extended X-ray absorption fine structure (EXAFS) spectra (Fig. 1g and Supplementary Table 1), the strained In_2S_3 sample showed a reduced In-S bond length (1.96 Å) as compared to that of pristine In_2S_3 sample (1.99 Å). Moreover, wavelet transform (WT) EXAFS plots in both K space and R space (Fig. 1h and Supplementary Fig. 12-17) show different In-O and In-S coordination in strained In_2S_3 as compared to reference samples. An obviously stronger electron paramagnetic resonance (EPR) signal at $g = 2.002$ was observed over strained In_2S_3 than pristine In_2S_3 (Supplementary Fig. 18), indicating a higher S-vacancy content in strained In_2S_3. A similar EPR signal was reported in defective metal sulfide[12]. All of the above characterization results indicate presence of In-O bonds together with sulfur vacancies in strained In_2S_3.

The light absorption properties of the as-prepared In_2S_3 catalysts were studied by UV−vis absorption spectroscopy. As shown in Fig. 2a, compared with pristine In_2S_3, the strained In_2S_3 displayed enhanced light absorption ability. The bandgap of the strained In_2S_3 was calculated to be about 1.76 eV (Supplementary Fig. 19), which was slightly smaller than that of pristine In_2S_3 (1.82 eV). Combined with ultraviolet photoelectron spectroscopy (UPS) measurements (Supplementary Fig. 20), it was inferred that the conduction band (CB) minimum of pristine In_2S_3 and strained In_2S_3 was located at −0.33 and −0.41 eV, respectively, as illustrated in Fig. 2b. It is important to note that the downshifted CB edge position for strained In_2S_3 can still meet the thermodynamic demand for CO_2 reduction[50–52]. As an important consideration for photocatalysis, the separation and transfer of photogenerated charge carriers were further investigated. As revealed in Fig. 2c, the strained In_2S_3 exhibited the lowest photoluminescence (PL) peak intensity relative to pristine In_2S_3, oxidized In_2S_3 and In_2O_3, indicating its lowest photoinduced charge carrier recombination rate. The same conclusion could be deduced from the surface photovoltage (SPV), transient photocurrent and electrochemical impedance spectroscopy measurements (Fig. 2d and Supplementary Fig. 21). Femtosecond transient absorption (fs-TA) spectroscopy was further performed to study the charge carrier dynamics. Figure 2e-f compared two-dimensional (2D) pseudocolor TA spectra for pristine In_2S_3 and strained In_2S_3, which displayed two distinctive absorption bands at 450-550 nm and 650-700 nm, respectively. Typical photobleaching peaks are observed in the pseudocolor plots of In_2S_3 (~450 nm) and strained In_2S_3 (~480 nm). These signals were assigned to the ground-state bleaching (GSB), reflecting the excited state relaxation. Figure 2g showed the fs-TA kinetic profiles at 475 nm for In_2S_3 and strained In_2S_3. With increasing probing time, an obvious decrease in TA intensity was detected, indicating a decrease of active photogenerated charges (Supplementary Fig. 22). The fs-TA spectra of In_2S_3 and strained In_2S_3 could be well fitted by a tri-exponential function and the fitting parameters are $\tau_1 = 3.26$ ps, $\tau_2 = 30.06$ ps, $\tau_3 = 69.82$ ps for In_2S_3, and $\tau_1 = 0.21$ ps, $\tau_2 = 5.15$ ps, $\tau_3 = 48.35$ ps for strained In_2S_3. The short-lived τ_1 corresponded to electron trapping by electron trapping state (e-TS), while the long-lived τ_2 and τ_3 were related to electron transition and recombination, respectively. Kinetic fitting gave the decay time of the ground-state bleaching (GSB) signal at 42.85 and 25.05 ps for In_2S_3 and strained In_2S_3, respectively, based on a triexponential decay function. The shorter GSB decay time in strained In_2S_3 resulted from charge carrier transfer to the atomically strained sites. The above results provide concerted evidences that the strained In sites can promote rapid transfer of photogenerated electrons.

Photocatalytic CO_2 reduction performance

The CO_2 photoreduction performance of strained In_2S_3 was evaluated under full spectrum or visible light (> 420 nm) irradiation in pure CO_2 without presence of any sacrificial reagents. The amount of photocatalyst used was first optimized in the photocatalytic CO_2 reduction reaction (Supplementary Fig. 23). Besides, we have conducted additional control experiments using pure Ar to replace CO_2 as the feeding gas. No CO_2 reduction products could be identified (Supplementary Fig. 24), eliminating the influence of carbon contamination during photoreaction. Figure 3a and Supplementary Fig. 25 show that the CO and CH_4 yields over strained In_2S_3 can reach 397.2 and 44.0 μmol $g_{catalyst}^{-1}$ (204.9 and 20.8 μmol $g_{catalyst}^{-1}$) after 4 h of photoreaction under full spectrum (visible) light illumination. The yield of CO is ca. 8.5 higher than that over pristine In_2S_3. In the meanwhile, water was oxidized to evolve molecular oxygen (Supplementary Fig. 26). As displayed in Fig. 3b, the strained In_2S_3 could still maintain appreciable CO and CH_4 yields under full spectrum and visible light irradiation (Supplementary Fig. 27) even if the reaction environment was switched from pure CO_2 to atmospheric CO_2 far superior to pristine In_2S_3 (Supplementary Fig. 28-29). The

https://doi.org/10.1038/s41467-025-57140-x

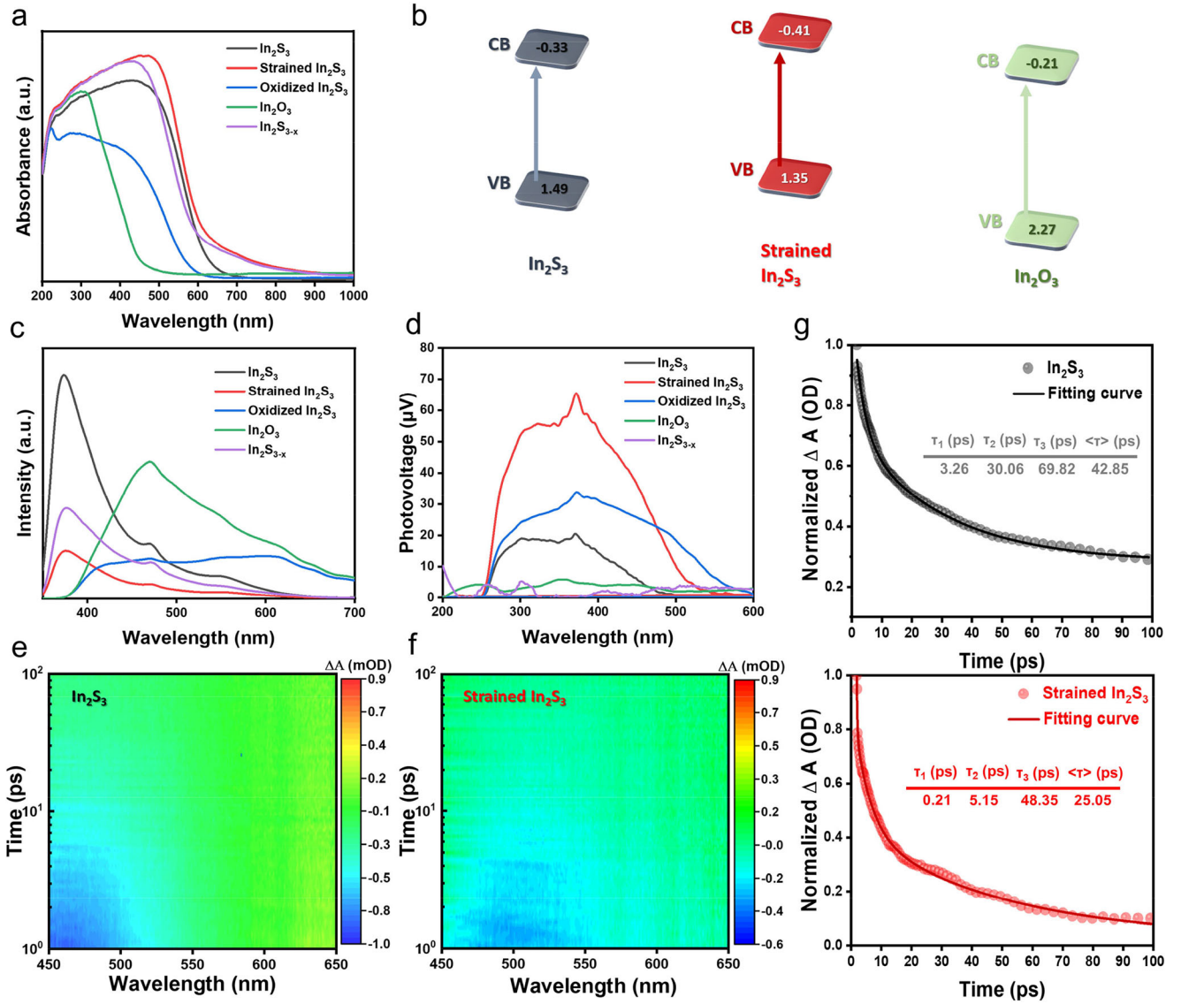

Fig. 2 | Insights into charge transfer dynamics. a UV–vis diffuse reflectance spectroscopy (DRS) spectra and **b** band structure of pristine In_2S_3, strained In_2S_3 and In_2O_3. **c** Steady-state PL spectra and **d** SPV signals over pristine In_2S_3, strained In_2S_3, oxidized In_2S_3, In_2O_3 and In_2S_{3-x}. 2D transient absorption pseudocolor plots for **e** pristine In_2S_3 and **f** strained In_2S_3. **g** The decay signals of pristine In_2S_3 and strained In_2S_3. Source data for Fig. 2a,c,d,g are provided as a Source Data file.

CO and CH_4 products were indeed produced via CO_2 photoreduction, verified by the $^{13}CO_2$ labeling experiments (Supplementary Fig. 30), and the presence of molecular O_2 had little influence on the CO_2 photoreduction reaction (Supplementary Fig. 31). The apparent quantum efficiency (AQE) of strained In_2S_3 was estimated and the result was shown in Supplementary Fig. 32, which well resembled the UV–vis absorption spectrum, reaching a maximum AQE of around 0.45% at 400 nm. The surface temperature of the strained In_2S_3 under visible light irradiation was at around 70 °C, measured using a thermographic technique (Supplementary Fig. 33). The control experiments disclosed that the CO_2 reduction reaction was completely terminated in dark at 70 °C or even at as high as 105 °C (Supplementary Fig. 34). Furthermore, when the photogenerated heat was removed by ice water, the strained In_2S_3 can still maintain nearly the same photocatalytic performance (Supplementary Fig. 34). These results reaffirmed the photoinduced CO_2 reduction reaction over strained In_2S_3. Besides high photocatalytic activity, the strained In_2S_3 also displayed decent photocatalytic stability: no significant photocatalytic activity decay was noticed after ten consecutive photoreaction cycles (Fig. 3c and Supplementary Fig. 35). The structure of the strained In_2S_3 could be well maintained after ten cycles of photoreaction based on a collection of characterizations including XRD, TEM, EPR and XPS (Supplementary Fig. 36), indicating its excellent stability in photoreaction. Compared to the reported In-based photocatalysts in literature, the strained In_2S_3 exhibited an obviously better photocatalytic CO_2 reduction performance in both pure and dilute CO_2 environment (Supplementary Table 2-3).

To understand the CO_2 photoreduction reaction mechanism over strained In_2S_3, in-situ Fourier transform infrared spectroscopy (FTIR) measurements were performed to probe the reaction intermediates. Carbonate species were found existing on the surface of strained In_2S_3 in humid CO_2 atmosphere under dark condition (Fig. 3d). The absorption peak at 1636, 1431 and 1287 cm^{-1} could be attributed to $*CO_2$, $*HCO_3^-$ and b-CO_3^{2-}, respectively. The observation of carbonate species and $*CO_2$ suggested that CO_2 could be adsorbed and activated over strained In_2S_3 under dark condition. Lowering CO_2 partial pressure reduced the intensities of infrared characteristic peaks (Fig. 3e). Compared with dark condition, several new absorption peaks at around 1576 cm^{-1}, 1135 cm^{-1} and 1070 cm^{-1}

https://doi.org/10.1038/s41467-025-57140-x

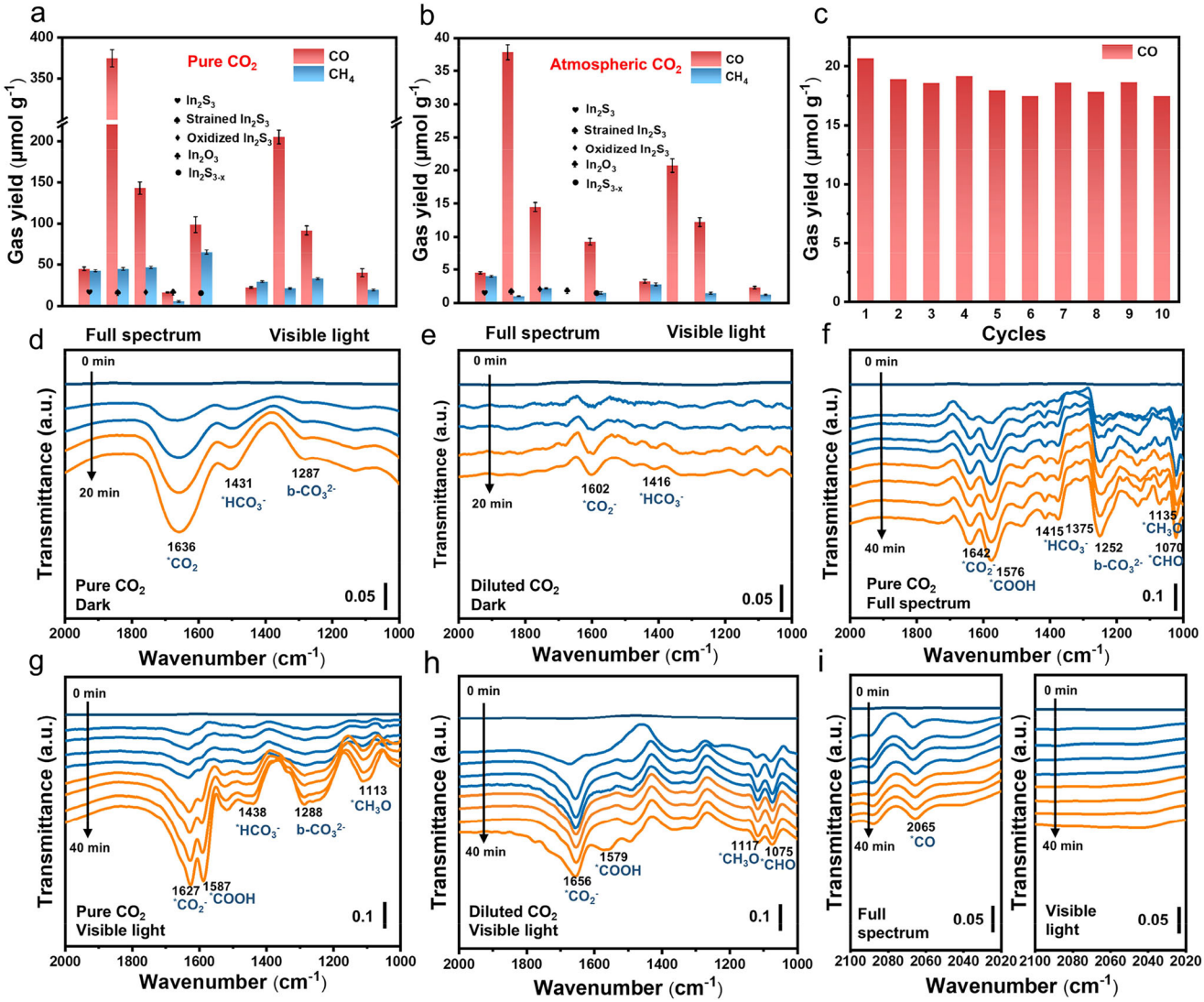

Fig. 3 | Photocatalytic CO_2 reduction performance. Product yields in CO_2 photoreduction reaction over various In_2S_3 photocatalysts conduced in **a** pure CO_2 and **b** ambient air. Error bars represent the standard deviation of three independent measurements. **c** Cyclic photocatalytic CO_2 reduction reaction conducted in ambient air for 40 hours. In-situ DRIFTS spectra recorded over strained In_2S_3 **d** under dark condition in pure CO_2, **e** under dark condition in ambient air, **f** under full spectrum irradiation condition in pure CO_2, **g** under visible light irradiation condition in pure CO_2, and **h** under visible light irradiation condition in ambient air. **i** The in-situ FTIR spectra in the wavenumber range from 2020 to 2100 cm^{-1} recorded over strained In_2S_3 under full spectrum irradiation condition in pure CO_2 (left) and under visible light irradiation condition in diluted CO_2 (right). Source data for Fig. 3a-i are provided as a Source Data file.

appeared under full spectrum (Fig. 3f) or visible-light (Fig. 3g) irradiation and their intensities increased with increasing light irradiation time, due to increased coverage of *COOH (a crucial intermediate for CO_2 reduction to CO or CH_4), *CH_3O and *CHO (the important intermediates for CO_2 reduction to CH_4), respectively. Besides, the *CO_2^- (1642 cm^{-1}), *HCO_3^- (1415 and 1375 cm^{-1}) and b-CO_3^{2-} (1252 cm^{-1}) absorption peaks also gradually strengthened with elongating light illumination time. Switching reaction environment from pure CO_2 to ambient air reduced the coverage (Fig. 3h) and changed the adsorption strength of CO_2 reduction intermediates. The *CO absorption peak at around 2076 cm^{-1} was clearly detected over strained In_2S_3 in pure CO_2 atmosphere under both visible and full spectrum light irradiation (Fig. 3i left), suggesting relatively strong *CO adsorption over strained In_2S_3 surface, which should be beneficial for the subsequent steps of protonation towards CH_4 formation. In ambient air environment, no obvious band near 2076 cm^{-1} was detected over strained In_2S_3, which explained the observed selective CO_2 photoreduction to CO.

Insight of the increased photocatalytic activity

To gain further theoretical insights, density functional theory (DFT) calculations were conducted to explore CO_2 adsorption and activation over strained In_2S_3. The strained In_2S_3 calculation model is shown in Fig. 4a, Supplementary Fig. 37 and Supplementary Data 1, 2 for details on the models, which was built based on a collection of characterization results. The CO_2 adsorption energy on the In site of pristine In_2S_3 was calculated to be −1.25 eV (Fig. 4b). The CO_2 adsorption energy over the In site was significantly more negative than that over the S and O site in strained In_2S_3, suggesting that formation of coordinatively unsaturated In sites is favorable for CO_2 adsorption[34]. It can be observed in Fig. 4c that strained In_2S_3 showed a much better CO_2 adsorption ability than pristine In_2S_3. In particular, the CO_2 adsorption curve of strained In_2S_3 rose significantly faster in the middle pressure range. At $P/P_0 = 1.0$, the CO_2 adsorption capacities of pristine In_2S_3, strained In_2S_3, oxidized In_2S_3, In_2O_3 and In_2S_{3-x} were 0.66, 3.54, 2.57, 1.05, and 2.25 $cm^3 g^{-1}$, respectively. Moreover, an upshift of the *p*-band center from -0.72 to -0.60 eV was also observed in strained In_2S_3 (Fig. 4d and Supplementary Fig. 38). It is

https://doi.org/10.1038/s41467-025-57140-x

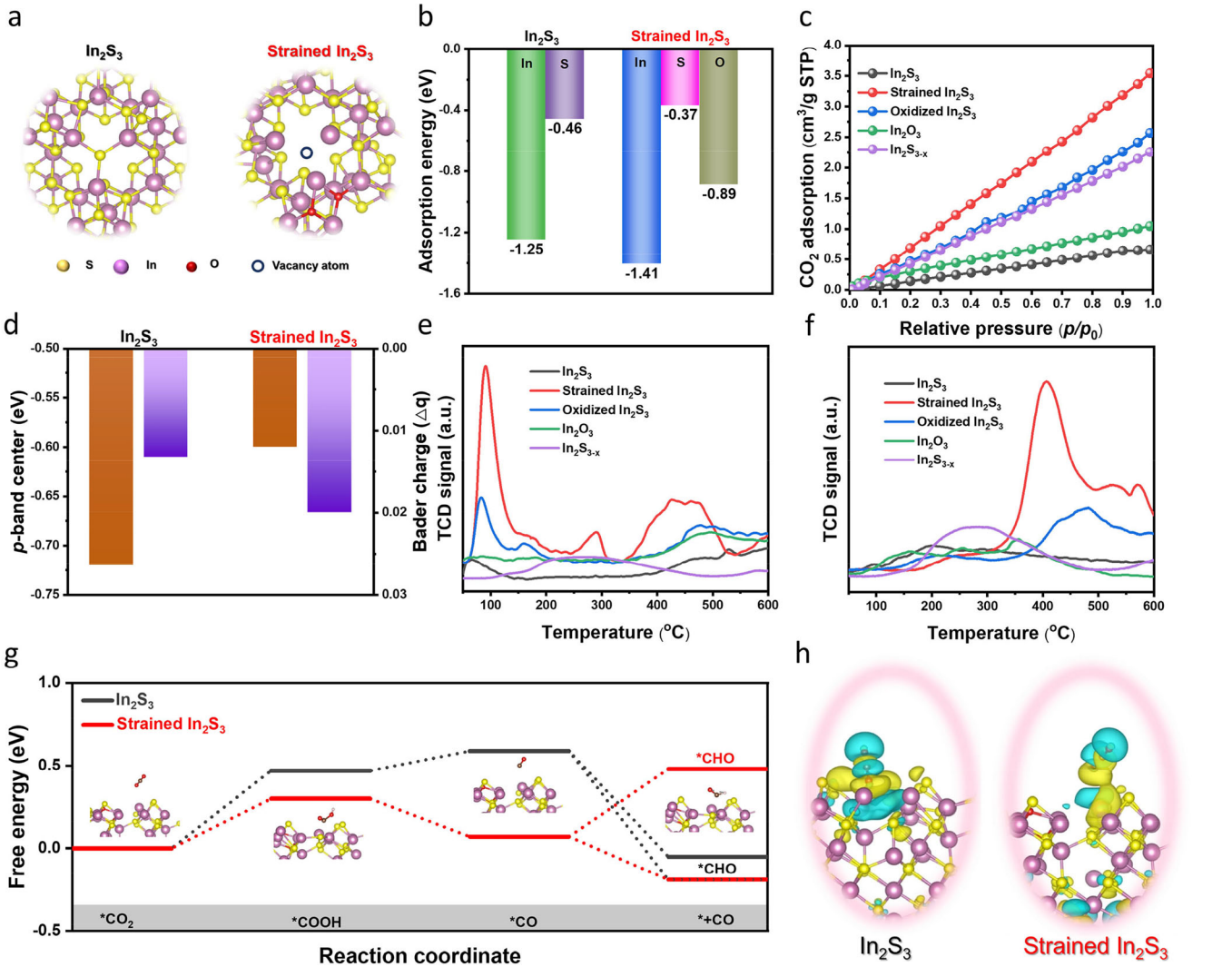

Fig. 4 | DFT study. a Schematic illustration showing the structural models for In_2S_3 and strained In_2S_3. **b** Calculated CO_2 adsorption energy on pristine In_2S_3 and strained In_2S_3. **c** CO_2 adsorption isotherms. **d** Calculated Bader charge and *p*-band-center. **e** CO_2 TPD curves. **f** CO TPD curves. **g** Calculated free energy diagrams for CO_2 reduction. **h** Calculated differential charge density of *COOH intermediate over pristine In_2S_3 and strained In_2S_3 surface. The insets a, g, and h show the DFT-optimized structures (In: purple, S: yellow, O: red, C: brown, and H: pink). Source data for b–f are provided as a Source Data file.

well established that the upshifted *p*-band center can push more antibonding states above the Fermi level, thus resulting in decreased occupation and stronger adsorbate bonding. The strained In site shifted the *p*-band center closer to the Fermi level and resulted in stronger surface bonding between the active sites and CO_2 molecules[53].

Temperature-programmed desorption (TPD) of CO_2 was performed to verify the enhanced CO_2 adsorption over strained In_2S_3 (Fig. 4e). The CO_2-TPD peak area for strained In_2S_3 was obviously larger than those for other In_2S_3 samples with a higher CO_2 desorption temperature, indicating that the strained In_2S_3 indeed could enhance CO_2 adsorption. Moreover, the CO TPD measurements indicated a concurrent stronger CO adsorption over strained In_2S_3, which was beneficial for *CO hydrogenation to form CH_4 in CO_2 photoreduction reaction (Fig. 4f). The reaction free energy and the structure configuration of each intermediate were simulated to illustrate the photocatalytic CO_2 reduction reaction mechanism (Supplementary Fig. 39 and Supplementary Table 4). Of note, the *COOH formation energy on strained In_2S_3 (0.30 eV) was more negative than that on In_2S_3 (0.47 eV), indicating that the atomically strained In sites can lower the energy required for the key conversion of $*CO_2$ to *COOH (Fig. 4g). Afterward, the downhill free energy profiles revealed that the formation of *CO from *COOH was more spontaneous over strained In_2S_3. Meanwhile, *CO protonation to *CHO on strained In_2S_3 had an energy barrier (0.48 eV) higher than that on pristine In_2S_3 (-0.05 eV), which can ensure a higher selectivity of CO generation on strained In_2S_3. As confirmed by differential charge densities over the *COOH-adsorbed structure models, higher concentrations of electrons were transferred to the near-surface region of strained In sites on strained In_2S_3 (Fig. 4h). Besides, water contact angle measurements (Supplementary Fig. 40) and DFT calculations (Supplementary Fig. 41) uncovered that the strained In_2S_3 could also tailor the rate-determining step for water reduction to boost proton generation (Supplementary Table 5).

Discussion

In summary, an atomically strained In_2S_3 photocatalyst has been rationally designed and successfully prepared by a wet-chemistry method, which exhibits high CO_2 photoreduction performance in both pure CO_2 and ambient air environment under full spectrum/visible light illumination. It is demonstrated that the strained In_2S_3 can significantly enhance photogenerated charge carrier separation and improve CO_2 adsorption/activation as characterized by a collection of

measurements and DFT calculations, as a result, greatly boosting CO_2 photoreduction performance.

Methods

Materials

$InCl_3{\cdot}4H_2O$ (AR, ≥99%), thioacetamide (TAA, AR, ≥99%), In_2O_3 (AR, ≥99%) granular NaOH (AR, ≥99%) were purchased from Aladdin Reagent Co. Ltd. Ethylene glycol was purchased from Shanghai Chemical Reagent Co., Ltd. All chemical reagents were used without further purification and ultrapure water (18.25 MΩ cm^{-1}) was used throughout the whole experiment.

Synthesis of In_2S_3

A total of 1.6 mmol of $InCl_3{\cdot}4H_2O$ was dissolved in 50 mL deionized water and stirred for 60 min. Then 2.4 mmol TAA was added and stirred for another 15 min. The obtained mixture was transferred into a 100 mL Teflon-lined stainless-steel autoclave, which was sealed and kept at 95 °C for 90 min. After the reaction, the autoclave was cooled down naturally, and the products were washed with deionized water and ethanol for several times and dried in ambient environment.

Synthesis of strained In_2S_3

A total of 1.6 mmol of $InCl_3{\cdot}4H_2O$ was dissolved in a mixed solvent containing 35 mL of deionized water and 15 mL of ethylene glycol and stirred for 60 min. Then, 2.4 mmol of TAA was added and stirred for another 15 min. The obtained mixture was transferred into a 100 mL Teflon-lined stainless-steel autoclave, which was sealed and kept at 95 °C for 90 min. After the reaction, the autoclave was cooled down naturally, and the products were washed with deionized water and ethanol for several times and dried in ambient environment.

Synthesis of oxidized In_2S_3

A total of 1.6 mmol of $InCl_3{\cdot}4H_2O$ was dissolved in 50 mL of ethylene glycol and stirred for 60 min. Then 2.4 mmol TAA was added and stirred for another 15 min. The obtained mixture was transferred into a 100 mL Teflon-lined stainless-steel autoclave, which was sealed and kept at 95 °C for 90 min. After the reaction, the autoclave was cooled down naturally, and the products were washed with deionized water and 1 M NaOH for several times and dried in ambient environment.

Synthesis of In_2S_{3-x}

The as-obtained In_2S_3 was rapidly heated at 300 °C for 2 min in Ar with 5% H_2 and then cooled to room temperature, and the products were washed with deionized water and ethanol for several times and dried in vacuum oven overnight

Characterization

The structural information of the as-prepared samples was analyzed by powder X-ray diffraction (XRD) on a D/MAX-RB diffractometer with Cu Kα radiation. The morphologies of the samples were examined by transmission electron microscopy (AC-TEM, JEM-ARM200F) at 200 kV. X-ray photoelectron spectroscopy (XPS) spectra were recorded on a Thermo VG Multilab 2000 spectrometer with Al Kα source. Ultraviolet photoelectron spectroscopy (UPS) measurements were performed on a Thermo Fisher ESCALAB 250Xi instrument with the He I radiation ($h\nu$ = 21.22 eV) source. EPR measurements were obtained using a Bruker model EMXPLUS 10/12 spectrometer. The optical properties of the samples were studied on a UV−vis-NIR spectrophotometer (UV-3600). The surface photovoltage (SPV) spectroscopy was performed on stable surface photovoltage spectrometer (PL-SPV/IPCE1000, Beijing Perfectlight). The equipment consists of a Xe lamp (CHF-XM-500 W), a monochromator (ZLolix SBP500) and a lock-in amplifier (SB830-DSP) with light chopper (SR540). The CO_2/CO adsorption properties were studied by performing CO_2-TPD and CO-TPD experiments on a Micromeritics AutoChem 2950HP. The CO_2 adsorption-desorption isotherms were measured on a Micromeritics ASAP2460. The transient photocurrent responses and the electrochemical impedance spectroscopy (EIS) spectra of the samples were recorded on an electrochemical workstation (CHI660C Instruments, China) with a three-electrode configuration in 30 mL 0.5 M Na_2SO_4 (aq.), where an Ag/AgCl (saturating KCl) electrode, a Pt plate and an indium tin oxide (ITO) glass coated with the sample worked as the reference, counter and working electrode, respectively. X-ray absorption near edge structure (XANES) spectra at the In *K*-edge were collected at the TLS16A1 station in the National Synchrotron Radiation Research Center (NSRRC). In foil was used as the reference. Data reduction, data analysis and extended X-ray absorption fine structure (EXAFS) fitting were performed using the Athena and Artemis software packages. In-situ Fourier transform infrared spectroscopy (FTIR) measurement was performed on a Vertex 70 FTIR spectrometer (Bruker). The sample to be measured was first pretreated inside the chamber in Ar at 120 °C for 30 min to clean the sample's surface. Afterwards, the background spectrum was then collected after the chamber's temperature was lowered to room temperature. Next, the gas (CO_2 or air 10 mL min^{-1}, H_2O/Ar 5 mL min^{-1}) was introduced into the reactor. After reaching the adsorption equilibrium in 30 min, the background spectrum was collected again. Subsequently, the light source (Xenon lamp with fiber optics, PLS-SXE300) was turned on, and the spectrum was recorded every 5 min under full spectrum or visible light irradiation.

Photocatalytic CO_2 reduction

Typically, 20 mg of photocatalyst was dispersed in 5 mL of deionized H_2O under ultrasonication. The above suspension was then dropped onto a quartz disc with a diameter of 5 cm and dried at 70 °C to obtain the photocatalyst-coated quartz disc. Afterwards, the quartz disc was placed in a custom-made reaction vessel (250 mL) filled with 5 mL of deionized H_2O on the bottom. Then, ~60 kPa of high purity CO_2 (99.999%) or compressed air was used as the CO_2 source. Light irradiation was provided by a PLS-SXE300D Xe lamp (Beijing Perfectlight) with a standard AM 1.5 G filter having an output light density of ~500 mW cm^{-2}, and the visible light was obtained by adding a filter (> 420 nm). Note that the distance from the lamp to the sample was ~10 cm. After adsorption equilibrium, the online gas-closed photocatalytic system (Labsolar-6A, Beijing Perfectlight) and gas chromatograph (GC-2014C, Shimadzu Corp., Japan) were used to quantify the gaseous products. The temperature of the gas-solid reactor was controlled at 298 ± 0.2 K by a recirculating cooling water system during light irradiation. The light intensity for CO_2 photoreduction reaction was measured by an optical power meter (PL-MW2000, Beijing Perfectlight).

Computational details

All density functional theory (DFT) calculations were performed in Vienna Ab initio Simulation Package (VASP) within the generalized gradient approximation (GGA) using the Perdew-Burke-Ernzerhof (PBE) formulation. The projected augmented wave (PAW) potentials were chosen to describe the ionic cores and valence electrons were taken into account using a plane wave basis set with a kinetic energy cutoff at 450 eV. For the optimization of both geometry and lattice size, the Brillouin zone integration was performed with 2 × 2 × 1 *Γ*-centered *k*-point sampling. The self-consistent calculations applied a convergence energy threshold of 10^{-5} eV. The equilibrium geometries and lattice constants were optimized with maximum stress on each atom within 0.02 eV $Å^{-1}$. In this work, a (3 × 3) supercell of In_2S_3 (111) and modified In_2S_3 (111) surface slabs were adopted, where the half bottom atomic layers were fixed for all calculations. To avoid interactions between periodic structures, ~15 Å vacuum space was inserted. The weak interaction was described by DFT + D3 method using empirical correction in Grimme's scheme. Spin polarization method was adopted to describe the magnetic system. The triaxial strain ε of

+3% was applied equally for all in-plane directions (A and B axes, compress strain), while a -9% strain was used in the perpendicular direction (C axis, tensile strain). The adsorption energy was calculated as: E_{ads} = E(*adsorbent) - E(*) - E(adsorbent), where E(*adsorbent), E(*) and E(adsorbent) represent the total energy of * adsorbent, * and adsorbent molecule, respectively. The Gibbs free energy for each elementary step was calculated as: G = E_{elec} + E_{ZPE} − TS, in which E_{elec} is the electronic energy at 0 K calculated by DFT, E_{ZPE} is the zero-point energy term, and T is the absolute temperature (here 298.15 K), S is the entropy.

Data availability

Source data are provided with this paper.

References

1. Xu, Y. et al. Engineering built-in electric field microenvironment of CQDs/g-C_3N_4 heterojunction for efficient photocatalytic CO_2 reduction. *Adv. Sci*. e2403607 (2024).
2. Wang, L., Wang, D. & Li, Y. Single-atom catalysis for carbon neutrality. *Carbon Energy* **4**, 1021–1079 (2022).
3. Ou, H. et al. Carbon nitride photocatalysts with integrated oxidation and reduction atomic active centers for improved CO_2 conversion. *Angew. Chem. Int. Ed.* **61**, e202206579 (2022).
4. Vu, N. N., Kaliaguine, S. & Do, T. O. Critical aspects and recent advances in structural engineering of photocatalysts for sunlight-driven photocatalytic reduction of CO_2 into fuels. *Adv. Funct. Mater.* **29**, 1901825 (2019).
5. Ou, M. et al. Amino-assisted anchoring of $CsPbBr_3$ perovskite quantum dots on porous g-C_3N_4 for enhanced photocatalytic CO_2 reduction. *Angew. Chem. Int. Ed.* **57**, 13570–13574 (2018).
6. Liu, L. et al. Tunable interfacial charge transfer in 2D-2D composite for efficient visible-light-driven CO_2 conversion. *Adv. Mater.* **35**, 2300643 (2023).
7. Ouyang, T. et al. Dinuclear metal synergistic catalysis boosts photochemical CO_2-to-CO conversion. *Angew. Chem. Int. Ed.* **57**, 16480–16485 (2018).
8. Zhou, Y. et al. Engineering 2D photocatalysts toward carbon dioxide reduction. *Adv. Energy Mater.* **11**, 2003159 (2021).
9. Zhao, Z. et al. Interfacial chemical bond and oxygen vacancy-enhanced In_2O_3/CdSe-DETA S-scheme heterojunction for photocatalytic CO_2 conversion. *Adv. Funct. Mater.* **33**, 2214470 (2023).
10. Zhang, X. et al. Photocatalytic conversion of diluted CO_2 into light hydrocarbons using periodically modulated multiwalled nanotube arrays. *Angew. Chem. Int. Ed.* **51**, 12732–12735 (2012).
11. Wang, K. et al. Unlocking the charge-migration mechanism in S-Scheme junction for photoreduction of diluted CO_2 with high selectivity. *Adv. Funct. Mater.* **34**, 2309603 (2023).
12. Yin, S. et al. Boosting water decomposition by sulfur vacancies for efficient CO_2 photoreduction. *Energy Environ. Sci.* **15**, 1556–1562 (2022).
13. Wang, S., Guan, B. Y., Lu, Y. & Lou, X. W. D. Formation of hierarchical In_2S_3-$CdIn_2S_4$ heterostructured nanotubes for efficient and stable visible light CO_2 reduction. *J. Am. Chem. Soc.* **139**, 17305–17308 (2017).
14. Xing, Z. et al. From one to two: in situ construction of an ultrathin 2D-2D closely bonded heterojunction from a single-phase monolayer nanosheet. *J. Am. Chem. Soc.* **141**, 19715–19727 (2019).
15. Wang, K. et al. Unveiling S-Scheme charge transfer pathways in In_2S_3/Nb_2O_5 hybrid nanofiber photocatalysts for low-concentration CO_2 hydrogenation. *Solar RRL* **7**, 2200963 (2022).
16. Yu, F., Jing, X., Wang, Y., Sun, M. & Duan, C. Hierarchically porous metal-organic framework/MoS_2 interface for selective photocatalytic conversion of CO_2 with H_2O into CH_3COOH. *Angew. Chem. Int. Ed.* **60**, 24849–24853 (2021).
17. Wang, K. et al. In situ-illuminated X-ray photoelectron spectroscopy investigation of S-Scheme Ta_2O_5/$ZnIn_2S_4$ core–shell hybrid nanofibers for highly efficient solar-driven CO_2 overall splitting. *Solar RRL* **6**, 2200736 (2022).
18. Bie, C., Zhu, B., Xu, F., Zhang, L. & Yu, J. In situ grown monolayer N-doped graphene on CdS hollow spheres with seamless contact for photocatalytic CO_2 reduction. *Adv. Mater.* **31**, e1902868 (2019).
19. Li, J. et al. Interfacial engineering of $Bi_{19}Br_3S_{27}$ nanowires promotes metallic photocatalytic CO_2 reduction activity under near-infrared light irradiation. *J. Am. Chem. Soc.* **143**, 6551–6559 (2021).
20. Liang, L. et al. Infrared light-driven CO_2 overall splitting at room temperature. *Joule* **2**, 1004–1016 (2018).
21. Jiao, X. et al. Defect-mediated electron-hole separation in one-unit-cell $ZnIn_2S_4$ layers for boosted solar-driven CO_2 reduction. *J. Am. Chem. Soc.* **139**, 7586–7594 (2017).
22. Li, Y. et al. Plasmonic hot electrons from oxygen vacancies for infrared light-driven catalytic CO_2 reduction on Bi_2O_{3-x}. *Angew. Chem. Int. Ed.* **60**, 910–916 (2021).
23. Zhu, S. et al. Selective CO_2 photoreduction into C_2 product enabled by charge-polarized metal pair sites. *Nano Lett* **21**, 2324–2331 (2021).
24. Li, X. et al. Selective visible-light-driven photocatalytic CO_2 reduction to CH_4 mediated by atomically thin $CuIn_5S_8$ layers. *Nat. Energy* **4**, 690–699 (2019).
25. Wang, K. et al. Atomic-level insight of sulfidation-engineered Aurivillius-related $Bi_2O_2SiO_3$ nanosheets enabling visible light low-concentration CO_2 conversion. *Carbon Energy* **5**, e264 (2022).
26. Maiti, S. et al. Engineering electrocatalyst nanosurfaces to enrich the activity by inducing lattice strain. *Energy Environ. Sci.* **14**, 3717–3756 (2021).
27. He, H. et al. Interface chemical bond enhanced ions intercalated carbon nitride/CdSe-diethylenetriamine S-scheme heterojunction for photocatalytic H_2O_2 synthesis in pure water. *Adv. Funct. Mater.* **34**, 2315426 (2024).
28. Liu, L. et al. Synergistic polarization engineering on bulk and surface for boosting CO_2 photoreduction. *Angew. Chem. Int. Ed.* **60**, 18303–18308 (2021).
29. Li, A. et al. Three-phase photocatalysis for the enhanced selectivity and activity of CO_2 reduction on a hydrophobic surface. *Angew. Chem. Int. Ed.* **58**, 14549–14555 (2019).
30. Li, X. et al. Ultrathin conductor enabling efficient IR light CO_2 reduction. *J. Am. Chem. Soc.* **141**, 423–430 (2019).
31. Liu, W. et al. Vacancy-cluster-mediated surface activation for boosting CO_2 chemical fixation. *Chem. Sci.* **14**, 1397–1402 (2023).
32. Bellotti, P. & Glorius, F. Strain-release photocatalysis. *J. Am. Chem. Soc.* **145**, 20716–20732 (2023).
33. Yue, X., Cheng, L., Li, F., Fan, J. & Xiang, Q. Highly strained Bi-MOF on bismuth oxyhalide support with tailored intermediate adsorption/desorption capability for robust CO_2 photoreduction. *Angew. Chem. Int. Ed.* **61**, e202208414 (2022).
34. Cao, X. et al. Engineering lattice disorder on a photocatalyst: photochromic BiOBr nanosheets enhance activation of aromatic C-H bonds via water oxidation. *J. Am. Chem. Soc.* **144**, 3386–3397 (2022).
35. Wang, Z. & Zhou, G. Lattice-strain control of flexible Janus indium chalcogenide monolayers for photocatalytic water splitting. *J. Phys. Chem. C* **124**, 167–174 (2019).
36. Miao, Y., Zhao, Y., Zhang, S., Shi, R. & Zhang, T. Strain engineering: a boosting strategy for photocatalysis. *Adv. Mater.* **34**, e2200868 (2022).
37. Feng, H. et al. Modulation of photocatalytic properties by strain in 2D BiOBr nanosheets. *ACS Appl. Mater. Interfaces* **7**, 27592–27596 (2015).
38. Huo, W., Xu, W., Guo, Z., Zhang, Y. & Dong, F. Motivated surface reaction thermodynamics on the bismuth oxyhalides with lattice strain for enhanced photocatalytic NO oxidation. *Appl. Catal. B* **284**, 119694 (2021).

39. Dai, D. et al. Strain adjustment realizes the photocatalytic overall water splitting on tetragonal zircon $BiVO_4$. *Adv. Sci.* **9**, e2105299 (2022).
40. Zhong, Q. et al. Strain-modulated seeded growth of highly branched black Au superparticles for efficient photothermal conversion. *J. Am. Chem. Soc.* **143**, 20513–20523 (2021).
41. Cai, X. et al. Synergism of surface strain and interfacial polarization on Pd@Au core–shell cocatalysts for highly efficient photocatalytic CO_2 reduction over TiO_2. *J. Mater. Chem. A* **8**, 7350–7359 (2020).
42. Yan, Y. et al. Tensile strain-mediated spinel ferrites enable superior oxygen evolution activity. *J. Am. Chem. Soc.* **145**, 24218–24229 (2023).
43. Hou, Z. et al. Lattice-strain engineering for heterogenous electrocatalytic oxygen evolution reaction. *Adv. Mater.* **35**, e2209876 (2023).
44. Wei, K. et al. Strained zero-valent iron for highly efficient heavy metal removal. *Adv. Funct. Mater.* **32**, 2200498 (2022).
45. Sabbah, A. et al. Boosting photocatalytic CO_2 reduction in a ZnS/$ZnIn_2S_4$ heterostructure through strain-induced direct Z-scheme and a mechanistic study of molecular CO_2 interaction thereon. *Nano Energy* **93**, 106809 (2022).
46. Huang, H. et al. Noble-metal-free ultrathin MXene coupled with In_2S_3 nanoflakes for ultrafast photocatalytic reduction of hexavalent chromium. *Appl. Catal. B* **284**, 119754 (2021).
47. Liu, Y. et al. Rapid room-temperature mechanosynthesis tensile-strained Bi_3O_4Br for robust photomineralization. *Catal. Commun.* **177**, 106638 (2023).
48. Hao, L. et al. Surface-halogenation-induced atomic-site activation and local charge separation for superb CO_2 photoreduction. *Adv. Mater.* **31**, e1900546 (2019).
49. Li, X. et al. Atomically strained metal sites for highly efficient and selective photooxidation. *Nano Lett.* **23**, 2905–2914 (2023).
50. Xiao, Y., Yao, C., Su, C. & Liu, B. Nanoclusters for photoelectrochemical water splitting: bridging the photosensitizer and carrier transporter. *EcoEnergy* **1**, 60–84 (2023).
51. Di, J. et al. Isolated single atom cobalt in Bi_3O_4Br atomic layers to trigger efficient CO_2 photoreduction. *Nat. Commun.* **10**, 2840 (2019).
52. Wu, X. et al. Identification of the active sites on metallic MoO_{2-x} nano-sea-urchin for atmospheric CO_2 photoreduction under UV, visible, and near-infrared light illumination. *Angew. Chem. Int. Ed.* **62**, e202213124 (2023).
53. Zhang, H. et al. Isolated cobalt centers on $W_{18}O_{49}$ nanowires perform as a reaction switch for efficient CO_2 photoreduction. *J. Am. Chem. Soc.* **143**, 2173–2177 (2021).

Acknowledgements

This work was financially supported by the National Nature Science Foundation of China (22378104, 52104254, 22173029, and 22308336), the City University of Kong Hong startup fund (9020003), ITF - RTH—Global STEM Professorship (9446006), JC STEM lab of Advanced CO_2 Upcycling (9228005) and Program for Innovative Teams of Outstanding Young and Middle-aged Researchers in the Higher Education Institutions of Hubei Province (T2023021).

Author contributions

Conceptional layout: K.W. and B.L. Investigation: K.W. Y.H., X.L., J.L., and B.L. Experimental data collection and processing: K.W. Computational simulation: K.W. and X.L. Manuscript co-writing: K.W. and B.L. Manuscript revising: K.W. Y.H., X.L., J.L., and B.L. Funding acquisition: K.W. Y.H., J.L., and B.L. Supervision: K.W. and B.L.

Competing interests

The authors declare no competing interests.

Additional information

Supplementary information The online version contains supplementary material available at https://doi.org/10.1038/s41467-025-57140-x.

Correspondence and requests for materials should be addressed to Kai Wang, Jun Li or Bin Liu.

Peer review information *Nature Communications* thanks Yanzhao Zhang, Liuqing Yang, and the other, anonymous, reviewer(s) for their contribution to the peer review of this work. A peer review file is available.